Research on the Gas–Solid Jet Flow and Erosion Wear Characteristics in Bottom Injecting Lance Used for Oxygen–Lime Powder Bottom Blowing Converter

SHAOYAN HU, RONG ZHU, DEYONG WANG, XIANGLONG LI, and GUANGSHENG WEI

Oxygen–lime powder bottom blowing converters have significant advantages in metallurgical performance, and have drawn more attention in recent studies. The key for oxygen–lime powder bottom blowing converter applications is to solve the problem of the furnace life. Erosion wear of the bottom injecting lance induced by a high velocity gas–solid jet inside the lance is an important factor for the furnace life but has rarely been studied. To reveal the gas–solid jet flow and erosion wear characteristics in the bottom injecting lance, a computational fluid dynamic model coupled with a discrete phase erosion model was established in the present work. The geometric dimension and boundary conditions of the lance were consistent with a commercial bottom injecting lance applied on a 120 ton converter. The simulated results were validated via a jet measurement experiment and an industrial experiment. The results show that the pressure loss in the lance of the gas–solid jet is much higher than that of pure gas jet, and the gas velocity at the lance outlet decreases after powder addition. Mixing powder into the gas has an obvious influence on the pressure variation curve and the velocity variation curve of the gas in the lance. The effect of the lance structure on jet flow and erosion wear was discussed in detail. On the premise that the total length of the lance remains constant, prolonging the shrink pipe length is helpful for reducing the pressure loss in lance. Simultaneously, the value of the maximum erosion wear and the area of the high wear rate region can be significantly reduced by prolonging the shrink pipe, which is vitally important for protecting the lance from being worn out by powder particles. The results of this work provide meaningful explorations and references for the design of converter bottom injecting lance.

I. INTRODUCTION

AN oxygen–lime powder bottom blowing converter is a smelting furnace developed for high-efficiency steelmaking, whose key feature is the use of a bottom injecting lance to simultaneously blow oxygen and lime powder through the bottom of the furnace, directly into the molten bath. Comparing the conventional oxygen top blowing converter, the oxygen bottom blowing converter provides a stronger stirring intensity and better thermodynamic and kinetic conditions for metallurgical reactions. Many production practices have confirmed that oxygen bottom blowing converters have significant advantages in terms of metallurgical performance, such as (1) decreased ferrous charge consumption (decreased T.Fe and dust)[1,2]; (2) good slag-metal reaction (dephosphorization and desulfurization)[3,4]; (3) a decreased gas content [O, N] in molten steel[5,6]; and (4) an improvement in the simultaneous endpoint achievement rate in the carbon content and temperature due to stable blowing.[7,8] However, the wide application of oxygen bottom blowing converters is limited because their furnace life is shorter than that of conventional converters, especially their furnace bottom life.[9] The destruction mechanisms of the furnace bottom induced by blowing oxygen have been widely studied and essentially revealed.[10–13] However, the erosion wear of the bottom injecting lance induced by powder injection has rarely been studied thus far. The authors performed an industrial experiment and found that a 2 mm thick copper pipe was worn out within 10 heats, which

SHAOYAN HU, DEYONG WANG, and XIANGLONG LI are with the School of Iron and Steel, Soochow University, Suzhou 215137, P.R. China. Contact e-mail: xlli202005@163.com RONG ZHU and GUANGSHENG WEI are with the School of Metallurgical and Ecological Engineering, University of Science and Technology Beijing, Beijing 100083, P.R. China. Contact e-mail: 1679324932@qq.com

illustrated that the erosion wear of the bottom injecting lance could not be ignored and should be given more attention. It is of paramount importance to gain more insights into the characteristics and severity of lance erosion to precisely identify the lance locations that are most susceptible to erosion and to predict the erosion rate.

The erosion wear induced by powder is closely related to the flow characteristics of the gas–solid jet. Many studies have confirmed that there are large differences between the gas–solid jet characteristics and pure gas jet characteristics even under the same gas flow rate.[14–16] Therefore, for the oxygen–lime powder injection lance, jet characteristics before and after lime powder addition need to be studied in detail separately. Limited by the experimental conditions and measurement methods, experiments can only provide limited data. Thus, jet characteristics were studied using the computational fluid dynamics (CFD) method in this study to obtain more abundant and intuitive results, and an experiment was conducted to validate the simulation results.

Many researchers have also used computational fluid dynamics methods to predict pipe erosion wear under different pipe geometric conditions and different flow conditions. Edwards et al.[17] investigated the effects of erosion in plugged tees and varying the bend radius in pipe elbows to develop procedures that could be applied within CFD codes for predicting pipe erosion. They claimed that the developed procedure was successful in predicting the fluid velocity through the investigated geometries with a good agreement in their prediction with experimental results for the particle penetration rate. McLaury et al.[18] developed a model to predict erosion rates in an annular flow for cases of horizontal and vertical pipe bend orientation. They found that the erosion was greater in magnitude in bends that were vertically orientated. A similar investigation was performed by Vieira et al.[19] Again, erosion was found to significantly increase in pipe bends that are vertically oriented. It was determined that increasing the pipe diameter led to a decrease in erosion rates. Wang and Shirazi[20] investigated the development of a CFD-based correlation that would allow for calculating the penetration rates where the bend radius is varied. The model showed a reasonable accuracy when compared with the experimental data. It was also concluded that using long radius bends helped to reduce the particle erosion in gas flows. Felten[21] provided an overview of erosion caused by solid particles in oil and gas pipe components, suggested methods of minimizing the erosion, and reviewed the various models available for predicting erosion.

Previous studies have shown that the flow and erosion wear characteristics of gas–solid jets in pipe systems can be predicted and described using the CFD method. However, it was determined that in the literature review, few studies have been performed on the bottom injecting lance used for oxygen–lime powder bottom blowing converters. Therefore, in this paper CFD modeling of erosion wear caused by solid lime particles carried by oxygen gas flowing in an oxygen–lime powder injection lance was conducted. Both the flow and erosion wear

characteristics in the lance were studied in detail. Based on the simulated results, the lance structure was optimized to improve the jet characteristics and reduce erosion wear, and then the specific effects of the lance structure on the erosion location and erosion rate were investigated. The simulated jet flow results were quantitatively validated via a gas–solid jet measurement experiment, and the simulated erosion wear results were qualitatively validated via industrial experiment phenomena.

II. COMPUTATIONAL MODELS

A. Geometric Models and Boundary Conditions

In this paper, a geometric model was established based on a commercial oxygen–lime powder injection lance installed on a 120 t oxygen bottom blowing converter. Figure 1 shows the 3D geometry of the lance, which is divided into five parts: the inlet pipe, elbow pipe, stable pipe, shrink pipe, and straight pipe. The inlet and outlet boundaries of the lance are also shown in Figure 1.
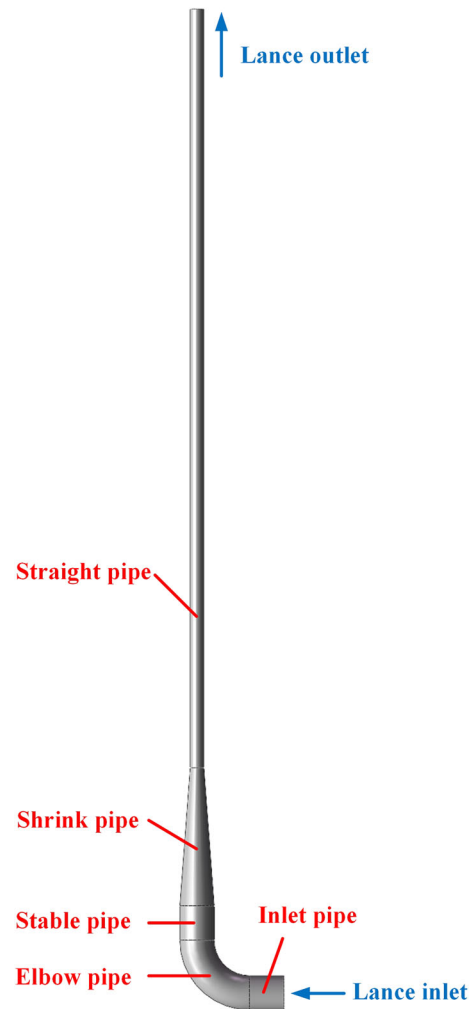

Fig. 1—3D geometry of the bottom injecting lance used for the oxygen–lime powder bottom blowing converter.

To eliminate the influence of the mesh quality on the computational results, a mesh independence test was performed. Four kinds of grid arrangements with different mesh qualities were established and simulated first, whose cell numbers were 491,305, 991,082, 1,530,021 and 1,989,985. As an example, the hexahedral grid structure of a mesh with 1,530,021 cells is shown in Figure 2. Mesh refinement was performed in the entire domain in order to capture the rapid fluctuation of jet flow characteristics and erosion wear. The minimum volume of the cells is only $1.5e-10$ m^3, and the maximum volume of the cells is $3.2e-9$ m^3. The minimum face area of the mesh element is $1.0e-7$ m^2, and the maximum face area of the mesh element is $2.5e-6$ m^2.

As mentioned above, the effect of the lance structure on the jet characteristics and erosion wear was studied in this paper. According to previous practices and the theoretical analysis, elbow pipes and straight pipes near shrink pipes are the locations that are most susceptible to erosion. Considering the actual installation conditions, the structure of the elbow pipe is hard to optimize and can only rely on material optimization and an increasing thickness. However, for straight pipes near shrink pipes, optimizing the structure of shrink pipes may be useful for reducing the erosion rate. Therefore, the length of the shrink pipe is the variable in studying the effect of the lance structure. The length of the straight pipe changes along with the length of the shrink pipe because the total length of the lance is maintained. The length of the shrink pipe in the original lance was 50 mm, and another five lengths were chosen to study the

effect of the lance structure. The geometric parameters of all six geometric models are shown in Table I. Apart from the lengths of the shrink pipe and the straight pipe, all other geometric parameters and mesh arrangements are constant.

All of the boundary conditions in the simulation were set up to agree with the actual situations in commercial applications and the experimental conditions used in this study. The boundary condition of the "mass flow inlet" was applied to the lance inlet, and the boundary condition of the "pressure outlet" was applied to the lance outlet. To accurately describe the flow and erosion behavior near the wall inside the lance, an enhanced wall treatment was applied to the lance walls. For the discrete phase particles, all the walls are set as reflecting walls.

In this paper, two kinds of jet characteristics were investigated: a pure gas jet before powder addition and a gas–solid jet after powder addition. Regardless of whether lime powder was added, the flow rate of the oxygen gas was kept at 20 Nm^3 min^{-1}. The basic properties of the oxygen gas are shown in Table II. The flow rate of the lime powder was 80 kg min^{-1}, the average particle diameter of the lime powder was 0.074 mm, and the density of the lime powder was 3320 kg m^{-3}, which were all consistent with the actual situation. The gauge pressure of the lance outlet was set to 0.0917 MPa, which is equal to the static pressure generated by molten steel in the furnace. It should be noted that the reference pressure in the simulation work and in this paper is 0.101 MPa (1 atm) for easy comparisons with experimental results.
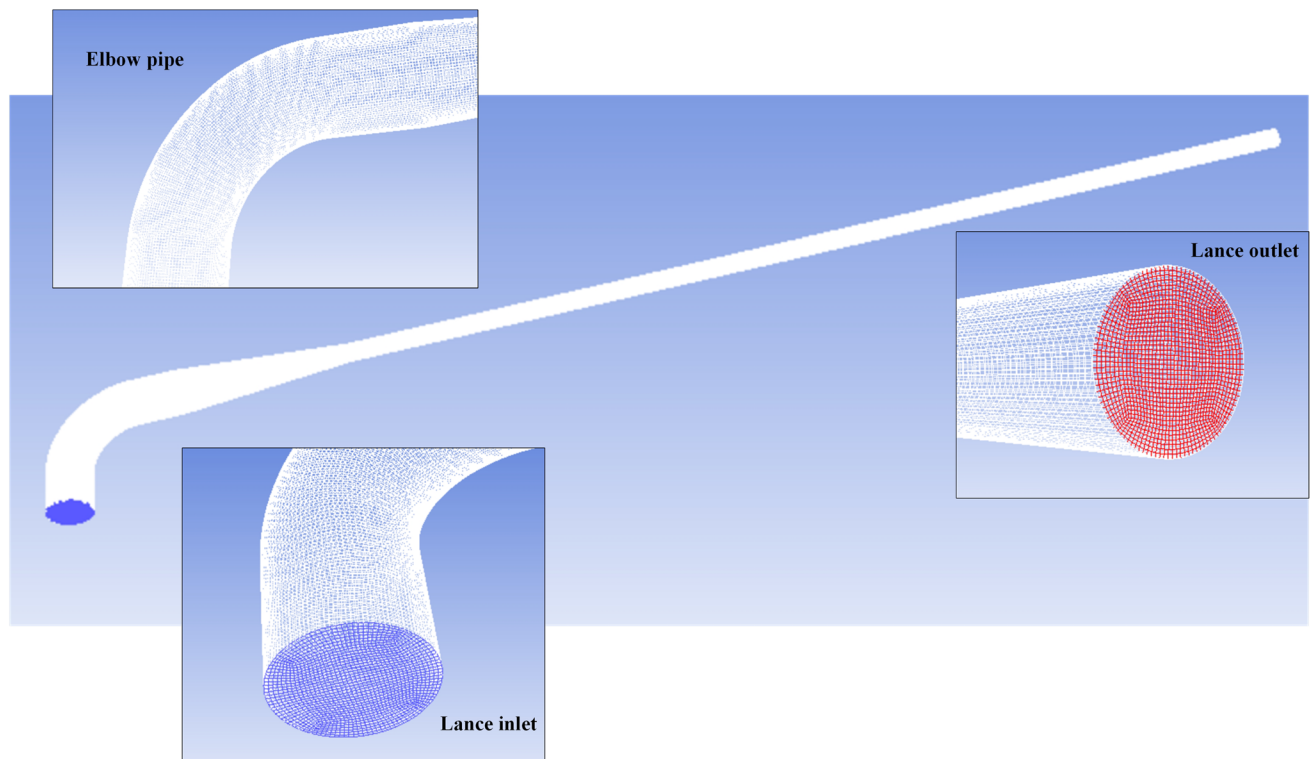

Fig. 2—Detailed grid structure of bottom injecting lance.

B. *Computation Procedure*

To compare the jet characteristics before and after the lime powder addition, cases without powder addition were simulated first, obtaining the flow field before powder addition as a contrast. Then the lime powder was released from the lance inlet, obtaining the flow field and erosion field after powder addition.

In the present simulation, the realizable k–ε model with enhanced wall treatment was used to model the turbulent flows, and the discrete phase model (DPM) with the erosion/accretion option was adopted to investigate the motion and erosion wear of lime powder. The thermophoretic force, Saffman lift force and pressure gradient force of the discrete phase were all taken into consideration. Gravity was also loaded into the model, whose direction was consistent with reality.

The steady, pressure-based solver and the implicit method were used to discretize and solve the model equations. The SIMPLE algorithm method was used to solve the pressure–velocity coupling. To improve the accuracy of the simulation results, a second-order upwind scheme was utilized to discretize the density, momentum, and turbulent kinetic energy equations, and the pressure equation was discretized using a standard scheme. Convergence was accepted when the residuals were less than 10^{-6} for the energy and 10^{-5} for all the other variables.

C. *Mathematical Models*

1. *Continuous phase flow equations*

In the present simulation, the gas phase was treated as a compressible ideal gas. The following governing equations were used:

Continuity equation

$$\frac{\partial \rho}{\partial t} + \nabla \cdot (\rho U) = 0 \qquad [1]$$

Momentum conservation equation

$$\frac{\partial}{\partial t}\rho U + \nabla \cdot (\rho U \times U) - \nabla \cdot (\mu_{\text{eff}} \nabla U)$$
$$= -\nabla P + \nabla[\mu_{\text{eff}}(\nabla U)] + B \qquad [2]$$

Energy equation

$$\frac{\partial}{\partial t}\rho H + \nabla \cdot \rho U H - \nabla \cdot \lambda \nabla T = \frac{\partial P}{\partial t} \qquad [3]$$

State equation of ideal gas

$$P = \rho R T \qquad [4]$$

where ρ is the average density of the fluid, t is time, U is the instantaneous velocity of fluid, P is the static pressure, μ_{eff} is the effective viscosity, B is the body force, H is the total enthalpy, λ is the thermal conductivity, T is the temperature, and R is the gas constant.

The realizable k–ε model with an enhanced wall treatment was used for modeling the turbulent flows in lance. Compared with the standard k–ε model and the RNG k–ε model, the realizable k–ε model improved the vortex viscosity and created a new equation for diffusion, whose turbulence kinetic energy (k) and dissipation rate (ε) equations are as follows:

$$\frac{\partial(\rho k)}{\partial t} + \frac{\partial(\rho k u_j)}{\partial x_i} = \frac{\partial}{\partial x_i}\left[\left(\mu + \frac{\mu_t}{\sigma_k}\right)\frac{\partial k}{\partial x_j}\right] + G_k + G_b - \rho_\varepsilon$$
$$- Y_M + S_k$$
$$[5]$$

$$\frac{\partial(\rho\varepsilon)}{\partial t} + \frac{\partial(\rho\varepsilon u_j)}{\partial x_j} = \frac{\partial}{\partial x_j}\left[\left(\mu + \frac{\mu_t}{\sigma_\varepsilon}\right)\frac{\partial \varepsilon}{\partial x_j}\right] + \rho C_1 S_\varepsilon$$
$$- \rho C_2 \frac{\varepsilon^2}{k + \sqrt{v\varepsilon}} + C_{1\varepsilon}\frac{\varepsilon}{k}C_{3\varepsilon}G_b + S_\varepsilon$$
$$[6]$$

where G_k is the turbulence kinetic energy generated by the laminar velocity gradients; G_b is the turbulence kinetic energy generated by buoyancy; Y_M is the contribution of the fluctuating dilatation in compressible turbulence to the overall dissipation rate; $C_{1\varepsilon}$, C_2 and $C_{3\varepsilon}$ are constants; σ_k and σ_ε are the turbulent Prandtl numbers for k and ε, respectively; and S_k and S_ε are used-defined source terms. The vortex viscosity (μ_t) was computed by combining k and ε as follows:

$$\mu_t = \rho C_\mu \frac{\varepsilon^2}{k} \qquad [7]$$

where C_μ is not a constant but is a function of the laminar strain and vorticity, which is the difference between the realizable k-ε model and other k–ε models. The model constants $C_{1\varepsilon}$, C_2, σ_k and σ_ε were usually given as follows: $C_{1\varepsilon}$ = 1.44, C_2 = 1.9, σ_k = 1.0 and σ_ε = 1.2.

2. *Discrete phase model*

The discrete phase model (DPM) in ANSYS Fluent was used to simulate the motion of lime powder carried by oxygen gas. The DPM model can compute the trajectories of the discrete phase as well as heat and mass transfer to/from them. The coupling between the phases and its impact on both the discrete phase trajectories and the continuous phase flow can be included.

ANSYS FLUENT predicts the trajectory of a discrete phase particle by integrating the force balance on the particle, which is written using a Lagrangian reference frame. This force balance equates the particle inertia with the forces acting on the particle and can be written as:

$$\frac{\mathrm{d}\vec{u}_p}{\mathrm{d}t} = \frac{\vec{u} - \vec{u}_p}{\tau_r} + \frac{\vec{g}(\rho_p - \rho)}{\rho_p} + \vec{F} \qquad [8]$$

where $\vec{F}$ is an additional acceleration (force/unit particle mass) term, $\frac{\vec{u} - \vec{u}_p}{\tau_r}$ is the drag force per unit particle mass and

$$\tau_r = \frac{\rho_p d_p^2}{18\mu}\frac{24}{C_d \text{Re}} \qquad [9]$$

No.	Diameter of the Inlet (mm)	Length of the Inlet Pipe (mm)	Curvature Radius of the Elbow Pipe (mm)	Length of the Stable Pipe (mm)	Length of the Shrink Pipe (mm)	Length of the Straight Pipe (mm)	Diameter of the Outlet (mm)
1	50	50	76	50	50	1250	20
2					100	1200	
3					200	1100	
4					300	1000	
5					400	900	
6					500	800	

Table II.   Basic Properties of the Gas Phase.

Name	Density (kg m^{-3})	Thermal Conductivity (w m^{-1} k^{-1})	Viscosity (kg m^{-1} s^{-1})
Oxygen	ideal gas	0.0246	1.919e−5

where τ_r is the particle relaxation time, $\vec{u}$ is the fluid phase velocity, $\vec{u}_p$ is the particle velocity, μ is the molecular viscosity of the fluid, ρ is the fluid density, ρ_p is the density of the particle, and d_p is the particle diameter. Re is the relative Reynolds number, which is defined as:

$$\mathrm{Re} = \frac{\rho d_p |\vec{u}_p - \vec{u}|}{\mu} \qquad [10]$$

The drag coefficient, C_d, is computed based on the spherical drag law, in which C_d is given by Eq. [11].

$$C_d = a_1 + \frac{a_2}{\mathrm{Re}} + \frac{a_3}{\mathrm{Re}^2} \qquad [11]$$

where a_1, a_2, and a_3 are constants that apply over a wide range of Re given by Morsi and Alexander.[22]

As mentioned above, for the discrete phase particles, all the lance walls are reflecting walls, meaning that the particles will be reflected by the wall after a collision. The particle rebounds off the walls with a change in its momentum as defined by the coefficient of restitution. The normal and tangent coefficients of restitution define the amount of momentum in the direction normal and tangent to the wall that is retained by the particle after a collision with the boundary, respectively. Both the normal and tangent coefficients of restitution were set up as polynomial functions of the impact angle in the present simulation works, as shown in Eqs. [12] and [13], respectively.[23,24]

$$y_N = 0.993 - 0.0307\alpha + (4.75e - 4)\alpha^2 - (2.61e - 6)\alpha^3 \qquad [12]$$

$$y_T = 0.988 - 0.029\alpha + (6.43e - 4)\alpha^2 - (3.56e - 6)\alpha^3 \qquad [13]$$

where α is the impact angle of the particle path with the wall face.

Table III.   Specific Setting Values for the Function of the Impact Angle.

Point	Angle (Deg)	Value
1	0	0
2	20	0.8
3	30	1
4	45	0.5
5	90	0.4

3. *Erosion model*

Based on the calculated flow field of the continuous phase and discrete phase through the model, ANSYS FLUENT can calculate the erosion wear. The particle erosion rate can be monitored at all wall boundaries. The general equation that calculates the rate of erosion is given as follows[25]:

$$R_{\mathrm{erosion}} = \sum_{p=1}^{N_{\mathrm{Particles}}} \frac{m_p C(d_p) f(\alpha) v^{b(v)}}{A_{\mathrm{face}}} \qquad [14]$$

where m_p is the particle mass flow rate, $C(d_p)$ is a function of particle diameter, α is the impact angle of the particle path with the wall face, $f(\alpha)$ is a function of the impact angle, v is the relative particle velocity, $b(v)$ is a function of the relative particle velocity, and A_{face} is the area of the cell face at the wall.

The values specified for the functions $C(d_p)$ and $b(v)$ were 1.8e−9 and 2.6, respectively, as recommended by Mazumder.[26–28] For the function of the impact angle $f(\alpha)$, a piecewise-linear function was adopted,[29–31] and the specific setting values are shown in Table III.

Importantly, it should be noted that the erosion wear rate calculated based on the above parameters is not universal because the actual erosion wear rate is related to many factors, such as the wall material, the surface quality and particle properties. The erosion wear magnitude obtained from the simulation work can only provide a data reference for qualitative study of the erosion rate and determine the effectiveness of the lance structure optimization.

III. MESH INDEPENDENCE TEST

The bottom injecting lance with structure No. 3 was chosen for the mesh independence test, whose shrink pipe length was 200 mm and straight pipe length was 1100 mm. To reveal the influence of the mesh quality on the computational results, the pressure distribution and velocity distribution of the pure gas jet inside the lance along the lance central axis are plotted in Figure 3. It should be noted that the axial distance of the horizontal ordinate starts from the entrance of the stable pipe and ends at the exit of the straight pipe. As shown in Figure 3, for the four tested grid arrangements, the mesh quality has little effect on the computational results. However, the enlarged details show that with an increasing cell number, both the inlet pressure and the outlet velocity of the gas jet decrease slightly. Considering the calculation accuracy and the time cost, a mesh with 1530021 cells was finally adopted in this paper.
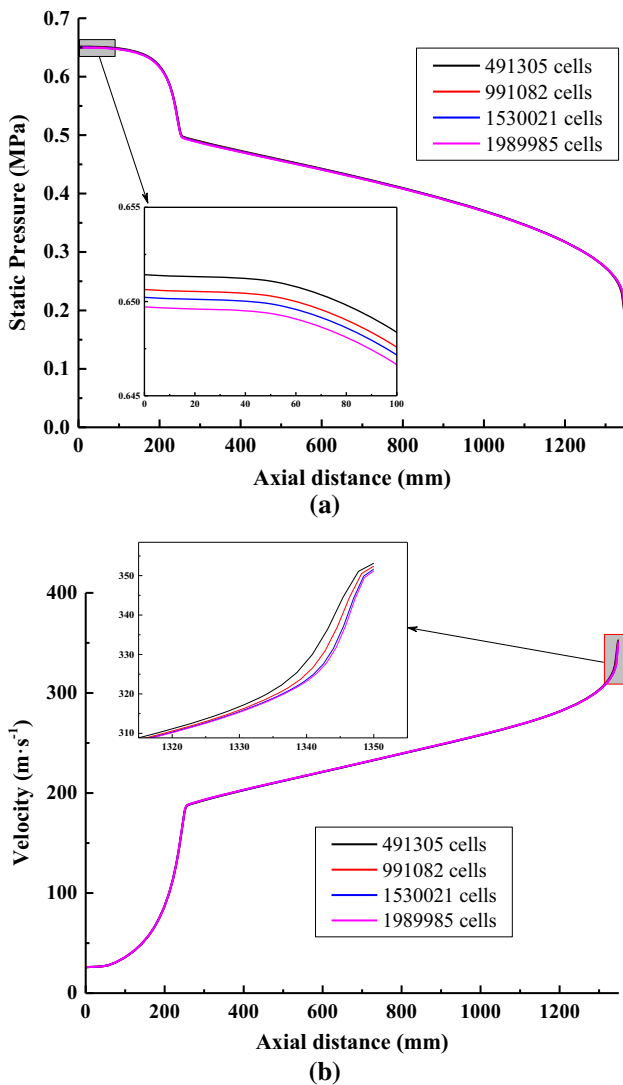

Fig. 3—Mesh independence test: (*a*) pressure distribution inside the lance, (*b*) velocity distribution inside the lance.

IV. EXPERIMENTAL APPARATUS FOR MODEL VALIDATION

An entire set of experimental equipment was built for jet characteristic measurement. Figure 4 shows a schematic diagram of the experimental apparatus and a real picture of the key devices. Oxygen was supplied by an oxygen storage tank, whose static pressure was greater than 1.6 MPa, which is essentially consistent with the commercial operating conditions. Lime powder was supplied using a lime powder storage tank. The flow rate of the lime powder can be adjusted by the regulating the valve installed at the bottom of the lime powder storage tank and monitored by the flowmeter of the powder installed at the powder pipeline. At the end of the powder pipeline, an oxygen–lime powder injection lance was installed, and a pressure gauge was set at the inlet of the lance to measure the inlet pressure of the gas jet and the gas–solid jet. The lane outlet was fixed in a steady pressure tank, in which the ambient pressure was kept at 0.0917 MPa, corresponding with the simulation. There was also a bag-type dust collector connected to the outlet of the steady pressure tank, which is not shown in the figure.

For the experiment performed in this research, the most useful data that can be obtained was the inlet pressure of the lance. The experimental scheme was the same as the simulation scheme. The inlet pressure values before and after powder addition with all six kinds of lance structures were measured experimentally.

V. RESULTS AND DISCUSSION

A. *Model Validation and Pressure Analysis*

Figure 5 shows the inlet pressure of the lance before and after powder addition. Both the simulated results and experimental results are shown. In Figure 5, "CFD: Gas jet" means the simulated pure oxygen gas jet before lime powder addition, "CFD: Gas–solid jet" means the simulated oxygen–lime powder mixed jet, "EXP: Gas jet" means the experimental oxygen gas jet before lime powder addition, and "EXP: Gas–solid jet" means the experimental oxygen–lime powder mixed jet.

Model validation will be discussed first. As shown in Figure 5, before lime powder addition, the simulated lance inlet pressure varies from 0.627 to 0.666 MPa with the change in the lance shrink pipe length, while the experimental pressure varies from 0.614 to 0.652 MPa; the deviation is approximately 1.5 pct. After lime powder addition, the simulated lance inlet pressure varies from 1.295 to 1.419 MPa, while the experimental pressure varies from 1.256 to 1.370 MPa; the deviation is approximately 2.5 pct. Undeniably, there exists a certain difference between the simulated results and the experimental results, and the difference increases with an increasing lance inlet pressure. However, the deviations under all conditions never exceed 3 pct in this research, which illustrates that the accuracy of the simulation results is acceptable.
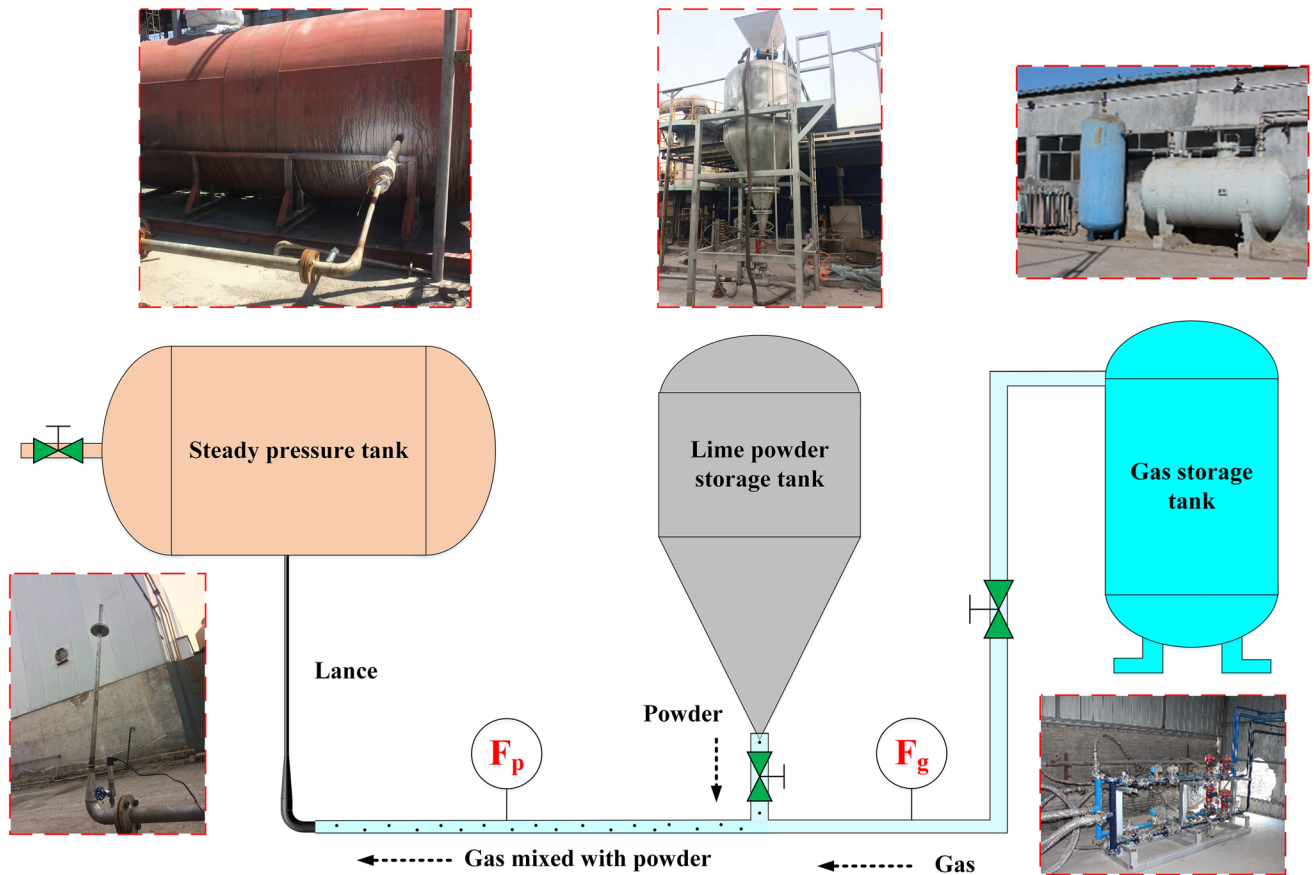
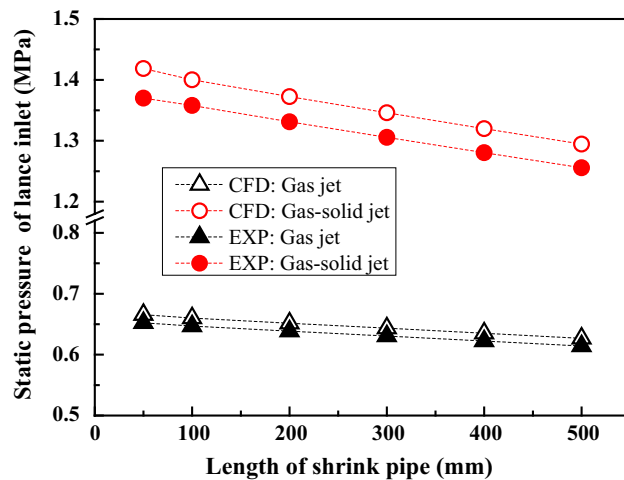Fig. 4—Schematic diagram of the experimental apparatus and real pictures of the key devices.

Fig. 5—Simulated and measured inlet pressure of the lance before and after powder addition.

mesh cell number. The greater the cell number is, the better the accuracy of the boundary layer simulation. However, it should also be noted that the influence of the mesh quality is very small, and its deviation is much smaller than the deviation between the experimental results and the simulated results. The main reason for the deviation may be related to the turbulence model, wall function, or other factors. Considering that the accuracy of the currently used computational model is acceptable, foundational exploration of the ultimate reason will be left for a further study.

After validating the model, the characteristics of the gas jet and gas–solid jet will be discussed in detail according to the simulation results. Two typical phenomena can be found from Figure 5. First, the inlet pressure of the gas–solid jet is much higher than that of the gas jet. For instance, when the length of the shrink pipe is 50 mm, the inlet pressure of the gas jet is 0.666 MPa, while the inlet pressure of the gas–solid jet is 1.419 MPa. The reason for the significant pressure difference is mainly the larger pressure loss of the gas–solid jet in the lance. Due to the coupling effect of the gas phase and powder particles, powder particles are driven to accelerate by the gas phase, which requires a greater energy consumption. Moreover, the friction resistance between the gas–solid jet and lance wall is larger, which also aggravates the pressure loss of the jet in the bottom blowing lance.

As shown in Figure 5, the experimental inlet pressures are always slightly smaller than the simulated results, regardless of whether the lime powder is added. Combined with the results shown in Figure 3(a), the mesh quality has little effect on the inlet pressure; that is, the simulated inlet pressure decreases with an increasing

Another phenomenon is that the inlet pressure decreases gradually with an increasing shrink pipe length, indicating a decrease in the pressure loss in the lance, especially for the gas–solid jet. For instance, when the shrink pipe length changes from 50 to 500 mm, the inlet pressure of the gas jet decreases from 0.666 to 0.627 MPa, and the inlet pressure of the gas–solid jet decreases from 1.419 to 1.295 MPa. A decrease in the inlet pressure is beneficial for industrial applications because it reduces the requirement of gas source pressure.

To analyze the pressure variation inside the lance, the static pressure of the gas phase inside the lance along the lance central axis is plotted in Figure 6. Figure 6(a) shows the static pressure of the gas phase before powder addition, and Figure 6(b) shows the static pressure of the gas phase after powder addition. In Figure 6, the axial distance of the horizontal ordinate starts from the entrance of the stable pipe and ends at the exit of the straight pipe, which is also the outlet of the lance. As mentioned above, the lengths of the stable pipes in all cases are constantly 50 mm, and the respective lengths of the shrink pipes in all cases are labeled in Figure 6.

Common features before and after powder addition are discussed first based on Figure 6. Starting from the entrance of the stable pipe, the static pressure of the gas phase essentially remains constant at first and then decreases sharply at the end of the shrink pipe. After entering the straight pipe, the static pressure first decreases at a gentle rate and then decreases sharply again at the end of the straight pipe. It is worth noting that in the shrink pipe of lance, the static pressure of the gas phase does not change immediately after entering the shrink pipe, but essentially remains constant at first, and the rapid pressure drop begins at the end of the shrink pipe, which can be seen from those cases with a longer shrink pipe.

The difference between cases before and after powder addition is mainly reflected in two aspects. (1) Compared with the cases before powder addition, the inlet pressure of the lance increases significantly and the outlet pressure of the lance increases slightly after powder addition. (2) Before powder addition, there is an obvious inflection point in the gas phase static pressure curve at the junction of the shrink pipe and straight pipe, and the decrease rate of the gas phase static pressure changes abruptly at this point, from a rapid decline to a relatively gentle decline; after powder addition, the obvious inflection point disappears, and the gas phase static pressure changes relatively gently at this position. Reasons for the first difference have been discussed above. The reason for the second difference is thought to be that, after powder addition, the powder enters the straight pipe from the shrink pipe at a certain angle due to inertia, which hinders the gas phase and occupies the flow area of the gas phase, as shown in Figure 7. Although the cross-sectional area of straight pipes is physically constant, due to the existence of powder particles the actual flow area for the gas phase seems to shrink gradually, which is similar to the change trend in shrink pipes; consequently, there is no obvious inflection point of the gas phase static pressure.

Another phenomenon that can be determined from Figure 6 is that regardless of whether powder is added, the gas phase static pressure at the lance outlet is higher than the static pressure generated by molten steel (0.0917 MPa). Before lime powder addition, the gas phase static pressure at the lance outlet is approximately 0.187 MPa. The gas phase static pressure then increases to approximately 0.236 MPa after lime powder addition. This means that the jet will continue to expand and accelerate after injection into molten steel, which helps to push away the molten steel near the lance outlet and protect the lance.

B. Velocity of the Jet

Figure 8 shows the effect of the shrink pipe length on the jet velocity at the lance outlet, including the velocity of the pure gas jet, the gas phase velocity of the gas–solid jet, and the particle velocity of the gas–solid jet. Before powder addition, the velocity of the pure gas jet at the lance outlet reaches 351.4 to 355.6 m s^{-1}. After
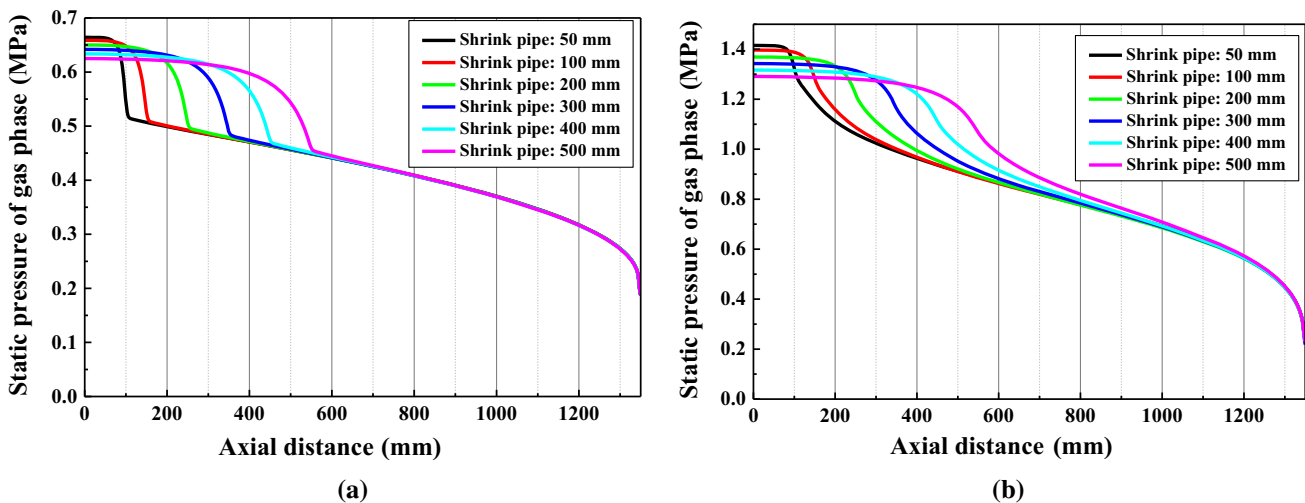
Fig. 6—Variation curve of the gas phase pressure inside the lance: (a) pure gas jet, (b) gas–solid jet.
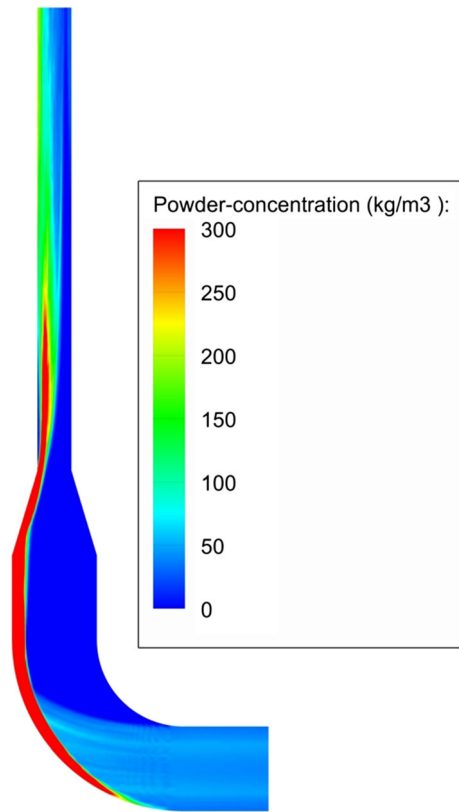
Fig. 7—Distribution of the powder concentration in the bottom injection lance.
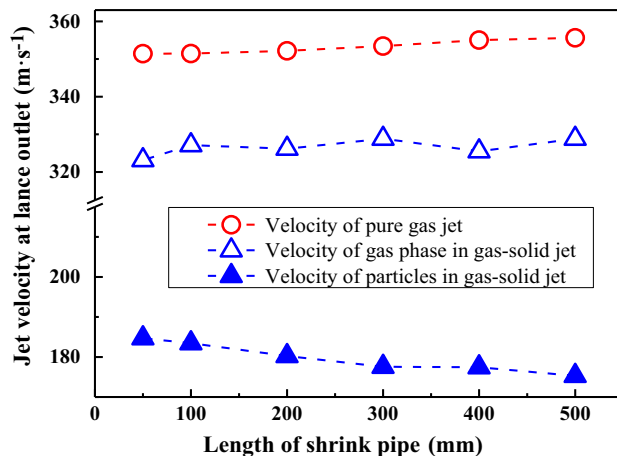

Fig. 8—Effect of the shrink pipe length on the jet velocity at the lance outlet.

To analyze the velocity variation inside the lance, the velocity magnitude of the gas phase inside the lance along the lance central axis is plotted in Figure 9. Figure 9(a) shows the velocity magnitude of the gas phase before powder addition, and Figure 9(b) shows the velocity magnitude of the gas phase after powder addition. Similar to Figure 6, the axial distance of the horizontal ordinate begins from the entrance of the stable pipe and ends at the exit of the straight pipe, which is also the outlet of the lance.

Before powder addition, there is a good correspondence between the gas velocity variation and the gas static pressure variation. The increasing trend of the gas velocity is consistent with the decreasing trend of the gas static pressure, which is induced by the conversion between pressure energy and kinetic energy. Similarly, an obvious inflection point also exists at the junction of the shrink pipe and straight pipe, and the increase rate of the gas velocity changes abruptly at this point from a rapid increase to a relatively gentle increase.

After powder addition, a difference between the gas velocity variation and the gas static pressure variation appears. Significant velocity fluctuation occurs in the straight pipe at the position near the shrink pipe, as shown in Figure 9(b). After entering the straight pipe, the gas continues to accelerate as if it is still in the shrink pipe. After accelerating to the maximum value, it begins to decelerate and then continues to accelerate at a slow rate. To explain the phenomenon of velocity fluctuation, velocity contours in the lance after powder addition are shown in Figure 10. Figure 10 shows that the velocity contours in the straight pipe near the shrink pipe are not well distributed. Because the powder particles move along the outside arc wall, after entering the straight pipe from the shrink pipe the particles continue to occupy the left flow area. As the powder particles move far away from the shrink pipe, particles gradually mix with the gas phase and spread to the central region, which makes the gas phase flow area decrease gradually, and the gas phase continues to accelerate, as in the shrink pipe. As noted above, Figure 9(b) shows the velocity of the central axis, which will pass through the low-speed area of the powder–gas mixing region, leading to a velocity decline after the maximum value. The gas phase and powder particles then gradually mix evenly and accelerate together.

To summarize, the special phenomenon of static pressure and velocity in straight pipes near shrink pipes after powder addition is attributed to the inertia of powder particles. Due to inertia, powder particles move along the outside arc wall of the elbow pipe and shrink pipe and then enter the straight pipe at a certain angle, occupying the flow area of the gas phase and hindering the flow trajectory of the gas phase.

Increasing the shrink pipe length is helpful for restraining the velocity fluctuation, as shown in Figure 9(b). Combined with Figure 10 for an analysis, thanks to the longer shrink pipe the gas phase and powder particles are mixed evenly before entering the straight pipe.
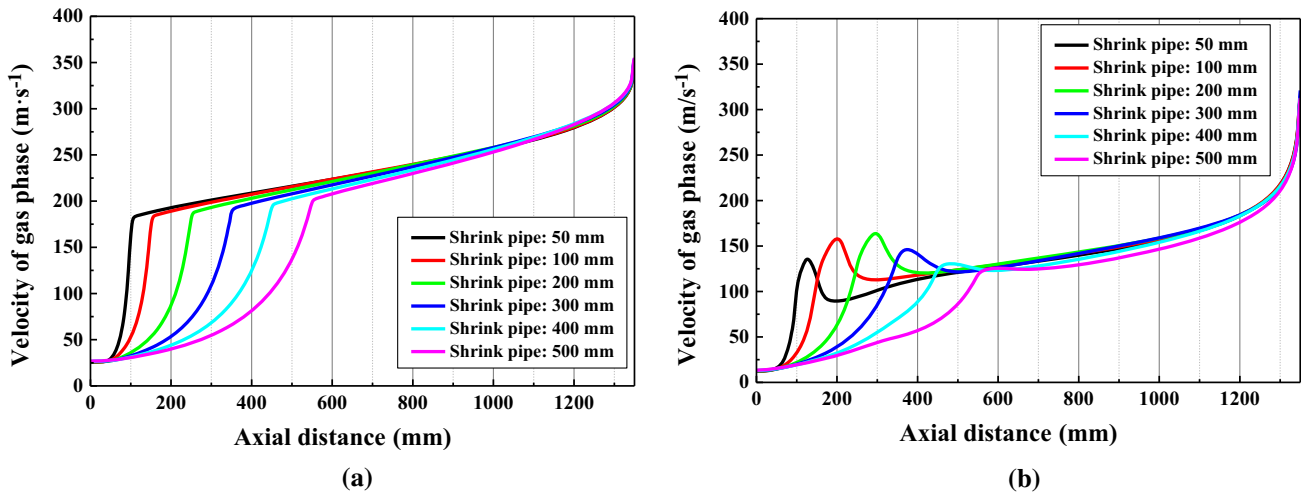
powder addition, the gas phase velocity drops to 323.2 to 328.8 m s^{-1}, which is related to the increase in the gas phase pressure at the lance outlet, as mentioned above. Meanwhile, the particles were driven by the gas phase and accelerated to 175.3 to 184.7 m s^{-1} at the lance outlet. In addition, the particle velocity of the gas–solid jet decreases slowly with an increasing shrink pipe length.

Fig. 9—Variation curve of the gas phase velocity inside the lance: (*a*) pure gas jet, (*b*) gas–solid jet.
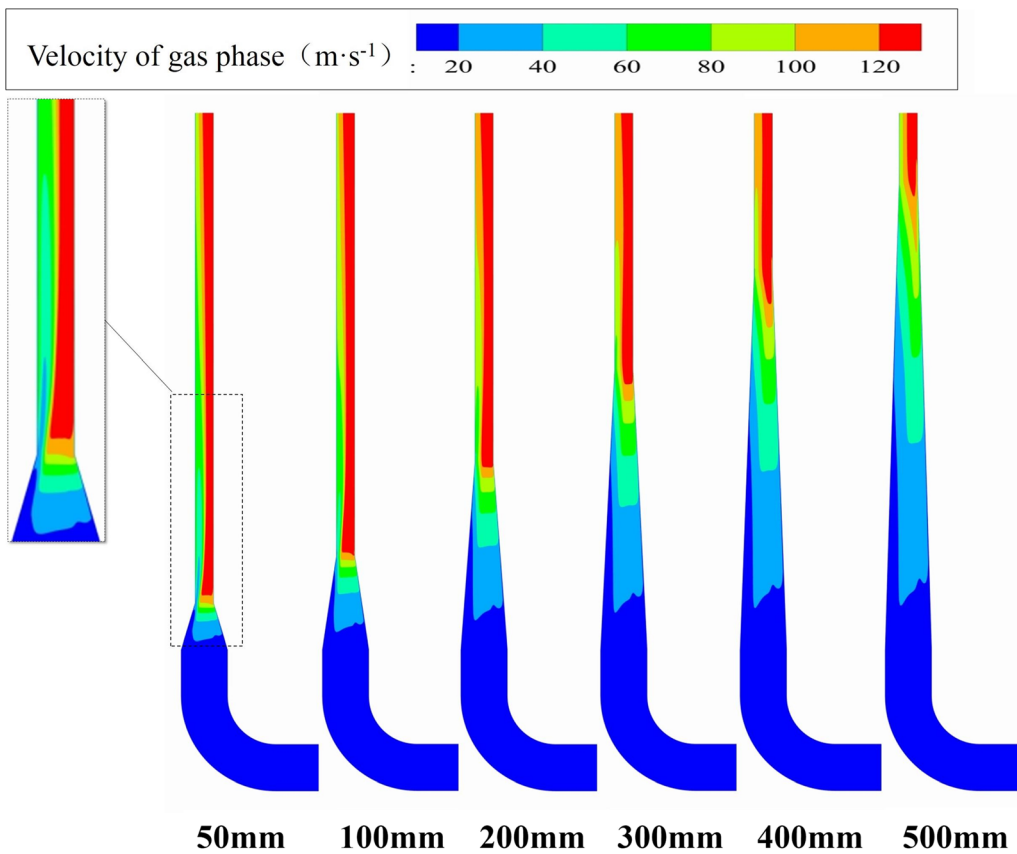

Fig. 10—Distribution of the gas phase velocity of the gas–solid jet inside the lance.

C. *Erosion Wear of the Lance*

To prevent the lance wall from being worn out by powder particles, it is vital to identify the weak point of the lance wall and determine a way to restrain the erosion wear. Figure 11 shows the simulated erosion wear rate contours of all six lances with different shrink pipe lengths. As shown in Figure 11, erosion wear mainly occurs in the elbow pipe and the straight pipe.

Because the elbow pipe is installed outside the furnace, it is easy to repair and replace. However, once the straight pipe is worn out, the lance will lose efficacy immediately and even cause dangerous accidents. In the straight pipe, the weak point occurs at the position near the shrink pipe, which is related to the particle trajectory, similar to what was discussed before. The powder particles move along the left wall of the shrink pipe, enter the straight
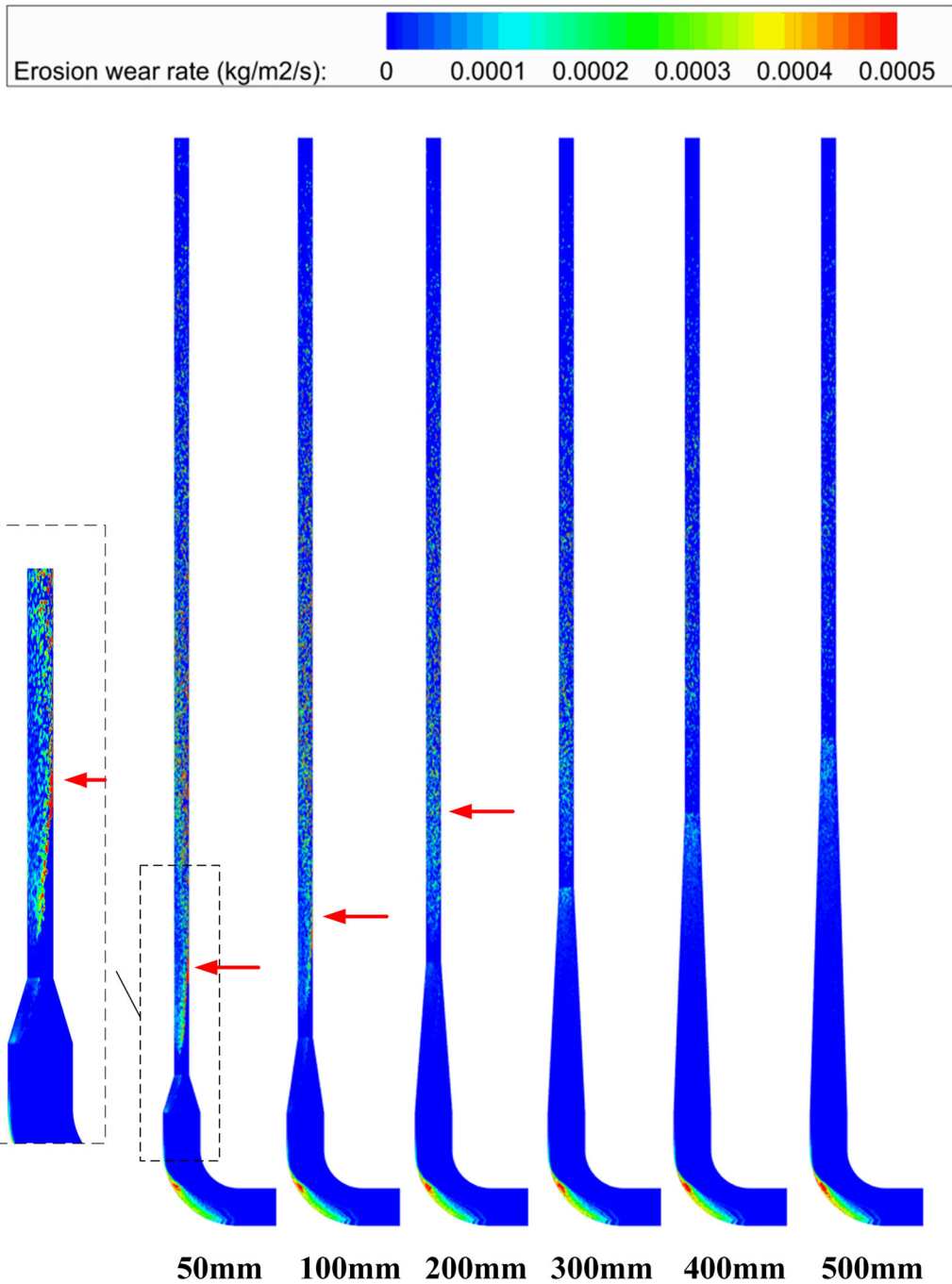
Fig. 11—Simulated erosion wear rate contour of lances with different shrink pipe lengths.

pipe at a certain angle, and then impact the right wall of the straight pipe, forming an obvious erosion wear region.

To verify the computation model, the simulated results were compared with the industrial experiment results. The industrial experiment was performed on a 50 ton EAF, and a powder injecting lance made of a 2 mm thick copper pipe was installed on the furnace wall, whose outlet was submerged under the molten bath, similar to the situation of the converter bottom injecting lance. The structure of the experimental lance was similar to that of simulated lance No. 1, whose shrink

pipe length was 50 mm, straight pipe length was 750 mm, and outlet diameter was 16 mm. The oxygen flow rate and lime powder flow rate of the experimental lance while smelting were 12 Nm^3 min^{-1} and 40 kg min^{-1}, respectively. Unfortunately, due to the very low hardness of copper, the lance was worn out by the lime powder with the 10th smelting heat, as shown in Figure 12. However, it presents the erosion wear characteristics of a powder injecting lance nicely. The distance between the worn-out position and the shrink pipe tail is approximately 150 mm, which is essentially consistent with the weak point obtained *via* numerical

simulations, indicating that the simulated results have a good guiding meaning for identifying the weak point of the lance.

Figure 11 also shows that with an increasing shrink pipe length, the area of the high erosion wear rate region obviously decreases, and the position of the maximum wear rate moves upward. When the shrink pipe length reaches greater than 200 mm, the conspicuous point of the maximum wear rate directed by the arrow in Figure 11 almost disappears.

After a qualitative analysis of erosion wear rate based on Figure 11, the values of the maximum wear rate and areas of high wear rate regions in the straight pipe are extracted and plotted in Figures 13 and 14. As shown in Figure 13, with an increasing shrink pipe length, the maximum wear rate in straight pipes decreases gradually. When the shrink pipe length increases from 50 to 500 mm, the maximum wear rate decreases from 0.00599 to 0.00112 kg m^{-2} s^{-1}, which decreases by 81.3 pct. In this study, the region with an erosion wear rate greater than 0.0005 kg m^{-2} s^{-1} is defined as a high wear rate region. Figure 14 shows that with an increasing shrink pipe length, the area of the high wear rate region in the straight pipe gradually decreases. When the shrink pipe length increases from 50 to 500 mm, the area of the high wear rate region decreases from 0.00423 to 0.0000985 m^2, which is a 97.7 pct decrease. Both the results of the maximum wear rate and the high wear rate region prove that increasing the shrink pipe length can effectively inhibit erosion wear in straight pipes, and the effect is quite remarkable.

VI. CONCLUSIONS

The flow characteristics of the gas–solid jet and erosion wear rate of the bottom injection lance are two important issues for oxygen–lime powder bottom blowing converters. To determine this, a computational fluid dynamic model coupling a discrete phase erosion model
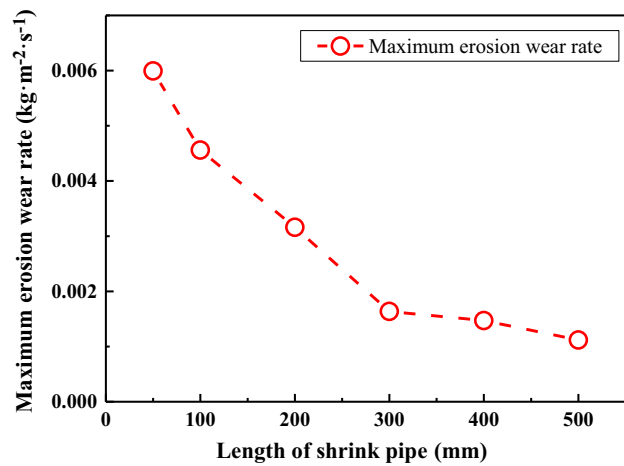

Fig. 13—Maximum wear rate in straight pipes of lances with different shrink pipe lengths.
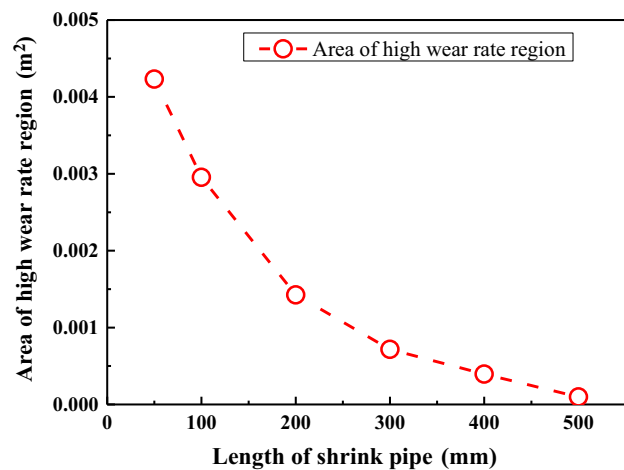

Fig. 14—Area of a high wear rate region in straight pipes of lances with different shrink pipe lengths.

Fig. 12—Lance worn out in the industrial experiment.

was utilized. The geometric model was established based on a commercial bottom injecting lance used in a 120 t converter. The effects of the lance structure on the jet characteristics and erosion wear were studied in detail. The findings can be summarized as follows:

1. An oxygen–lime powder injection experiment was conducted in this research. The applicability of the numerical simulation model was validated by the good agreement between the simulated inlet pressure and the experimental inlet pressure.
2. Under the premise of a constant gas flow rate, the pressure of the gas–solid jet at the lance inlet is much higher than that of the pure gas jet. In addition, the inlet pressure decreases with an increasing shrink pipe length, indicating a decrease in the pressure loss in the lance, especially for the gas–solid jet, which is beneficial for industrial applications.
3. Before powder addition, there is an obvious inflection point in the gas phase static pressure curve at the junction of the shrink pipe and the straight pipe, and the decrease rate in the gas phase static pressure changes abruptly at this point, from a rapid decline to a relatively gentle decline. After powder addition, the obvious inflection point disappears, and the gas phase static pressure changes relatively gently at this position.
4. Before powder addition, the velocity of the pure gas jet at the lance outlet reaches 351.4 to 355.6 m s^{-1}. After powder addition, the gas phase velocity drops to 323.2 to 328.8 m·s^{-1}, while the particles are driven by the gas phase and accelerate to 175.3 to 184.7 m·s^{-1} at the lance outlet. In addition, the particle velocity of the gas–solid jet decreases slowly with an increasing shrink pipe length.
5. For the structure type of the bottom injecting lance studied in this paper, erosion wear mainly occurs in the elbow pipe and the straight pipe, which has been well verified by industrial results. In the straight pipe, a weak point occurs at the position near the shrink pipe, which is related to the particle trajectory. Increasing the shrink pipe length can, simultaneously, significantly reduce the value of the maximum wear rate and the area of the high wear rate region in a straight pipe, which is vitally important for protecting the lance from being worn out by powder particles.

CONFLICT OF INTEREST

On behalf of all authors, the corresponding author states that there are no conflicts of interest.

REFERENCES

1. H. Sun, Y. Liu, and M. Lu: *Ironmak. Steelmak.*, 2016, vol. 43, pp. 697–704.
2. Y. Li: *Iron Steel*, 1980, vol. 27, pp. 1–9.
3. Y. Zhong, L. Guan, and M. Lin: *Iron Steel*, 1979, vol. 26, pp. 34–44.
4. G. Wimmer, K. Pastucha, and E. Wimmer: *The 6th International Congress on Science and Technology of Steelmaking*, 2015.
5. M. Abe, Y. Kishimoto, and S. Takeuchi: *Tetsu-to-Hagane*, 2009, vol. 82, pp. 743–48.
6. M. Lv, R. Zhu, and L. Yang: *Steel Res. Int.*, 2019, vol. 90, pp. 1–7.
7. T. Kosukegawa, T. Imai, and F. Sudo: *Proc. of International Symposium on Modern Developments in Steelmaking*, NML, Jamshedpur, 1981.
8. S. Sun, D. Liao, and N. Pyke: *Iron Steel Tech.*, 2008, vol. 5, pp. 36–42.
9. D. Liao, S. Sun, and S. Waterfall: *The 6th International Congress on Science and Technology of Steelmaking*, 2015.
10. R. Ruther and P. Opel: *Neue Hutte*, 1978, vol. 23, pp. 254–57.
11. N.B. Ballal and A. Ghosh: *Metall. Trans. B*, 1981, vol. 12, pp. 525–34.
12. K. Scheidig, R. Guther, and G. Fromer: *Neue Hutte*, 1980, vol. 25, pp. 207–10.
13. I.V. Belov: *Izv. Akad. Nauk. SSSR*, 1997, vol. 4, pp. 16–21.
14. K. Hishida, K. Kaneko, and M. Maeda: *Trans. Jpn. Soc. Mech. Eng. B*, 1985, vol. 51, pp. 2330–33.
15. S. Yu and T. Umekage: *Trans. Jpn. Soc. Mech. Eng. B*, 1994, vol. 60, pp. 1152–56.
16. S. Yu, S. Katamaki, H. Kohno, and T. Umekage: *Trans. Jpn. Soc. Mech. Eng. B*, 1998, vol. 64, pp. 29–35.
17. J. Edwards, B. McLaury, and S. Shirazi: *J. Energy Resour.*, 2001, vol. 123, pp. 277–84.
18. B. McLaury, S. Shirazi, V. Viswanathan, and Q. Mazumder: *J. Energy Resour.*, 2011, vol. 133, pp. 23–32.
19. R. Viera, N. Kesena, B. McLaury, and S. Shirazi: *ASME 2012 International Mechanical Engineering Congress and Exposition*, 2012.
20. J. Wang and S. Shirazi: *J. Energy Resour.*, 2003, vol. 125, pp. 26–34.
21. F. Felten: *Proceedings of the ASME 2014 4th Joint US-European Fluids Engineering Division Summer Meeting*. 2014.
22. S. Morsi and A. Alexander: *J. Fluid Mech.*, 1972, vol. 55, pp. 193–208.
23. A. Fonder, M. Thew, and D.A. Harrison: *Wear*, 1998, vol. 216, pp. 184–93.
24. Y. Guan, C. Xiong, H. Diao, K. Peng, and D. Xu: *Oil Field Equipment*, 2016, vol. 45, pp. 16–18.
25. Fluent 13.0 user's guide: *Flunt Inc.*, Lebanon, USA, 2010.
26. Q. Mazumder: *Vdm Verlag Dr Müller*, 2009.
27. Q. Mazumder, S. Zhao, and K. Ahmed: *Model. Simul. Eng.*, 2015.
28. Q. Mazumder, K. Hassn, A. Kamble, and V. Nallamothu: *Experimental and Computational Multiphase Flow*, 2020.
29. B. Krupicz, W. Tarasiuk, J. Napirkowski, and K. Ligier: *Tribologia*, 2017, vol. 273, pp. 85–90.
30. Y. Oka, H. Ohnogi, T. Hosokawa, and M. Matsumura: *Wear*, 1997, vol. 203, pp. 573–79.
31. T. Ping, Y. Jian, J. Zheng, I. Wong, S. He, J. Ye, and G. Ou: *Eng. Fail. Anal.*, 2009, vol. 16, pp. 1749–56.